



**HAL**  
open science

# Characterization of Thermal-infrared Dust Emission and Refinements to the Nucleus Properties of Centaur 29P/Schwassmann–Wachmann 1

Charles Schambeau, Yanga Fernández, Nalin Samarasinha, Maria Womack, D. Bockelée-Morvan, Carey Lisse, Laura Woodney

► **To cite this version:**

Charles Schambeau, Yanga Fernández, Nalin Samarasinha, Maria Womack, D. Bockelée-Morvan, et al.. Characterization of Thermal-infrared Dust Emission and Refinements to the Nucleus Properties of Centaur 29P/Schwassmann–Wachmann 1. *The Planetary Science Journal*, 2021, 2 (4), pp.126. 10.3847/PSJ/abfe6f . hal-03425738

**HAL Id: hal-03425738**

**<https://hal.science/hal-03425738>**

Submitted on 11 Nov 2021

**HAL** is a multi-disciplinary open access archive for the deposit and dissemination of scientific research documents, whether they are published or not. The documents may come from teaching and research institutions in France or abroad, or from public or private research centers.

L'archive ouverte pluridisciplinaire **HAL**, est destinée au dépôt et à la diffusion de documents scientifiques de niveau recherche, publiés ou non, émanant des établissements d'enseignement et de recherche français ou étrangers, des laboratoires publics ou privés.



# Characterization of Thermal-infrared Dust Emission and Refinements to the Nucleus Properties of Centaur 29P/Schwassmann–Wachmann 1

Charles A. Schambeau<sup>1,2</sup> , Yanga R. Fernández<sup>1,2</sup> , Nalin H. Samarasinha<sup>3</sup> , Maria Womack<sup>2,4</sup> ,

Dominique Bockelée-Morvan<sup>5</sup> , Carey M. Lisse<sup>6</sup> , and Laura M. Woodney<sup>7</sup>

<sup>1</sup> Florida Space Institute, University of Central Florida, 12354 Research Parkway, Partnership 1, Orlando, FL 32826, USA; [charles.schambeau@ucf.edu](mailto:charles.schambeau@ucf.edu)

<sup>2</sup> Department of Physics, University of Central Florida, Orlando, FL 32816, USA

<sup>3</sup> Planetary Science Institute, Tucson, AZ 85719, USA

<sup>4</sup> National Science Foundation, Alexandria, VA 22314 USA

<sup>5</sup> LESIA, Observatoire de Paris, PSL Research University, CNRS, Sorbonne Université, Université de Paris, 5 place Jules Janssen, F-92195 Meudon, France

<sup>6</sup> Johns Hopkins University, Applied Physics Laboratory, Laurel, MD 20723, USA

<sup>7</sup> Department of Physics, California State University, San Bernardino, San Bernardino, CA 92407, USA

Received 2020 October 1; revised 2021 May 3; accepted 2021 May 3; published 2021 July 15

## Abstract

We present analyses of Spitzer observations of 29P/Schwassmann–Wachmann 1 using 16  $\mu\text{m}$  IRS “blue” peak-up (PU) and 24 and 70  $\mu\text{m}$  MIPS images obtained on UT 2003 November 23 and 24 that characterize the Centaur’s large-grain (10–100  $\mu\text{m}$ ) dust coma during a time of non-outbursting “quiescent” activity. Estimates of  $\epsilon\beta$  for each band (16  $\mu\text{m}$  ( $2600 \pm 43$  cm), 24  $\mu\text{m}$  ( $5800 \pm 63$  cm), and 70  $\mu\text{m}$  ( $1800 \pm 900$  cm)) follow the trend between nucleus size versus  $\epsilon\beta$  that was observed for the WISE/NEOWISE comet ensemble. A coma model was used to derive a dust production rate in the range of 50–100  $\text{kg s}^{-1}$ . For the first time, a color temperature map of SW1’s coma was constructed using the 16 and 24  $\mu\text{m}$  imaging data. With peaks at  $\sim 140$  K, this map implies that coma water-ice grains should be slowly sublimating and producing water gas in the coma. We analyzed the persistent 24  $\mu\text{m}$  “wing” (a curved southwestern coma) feature at 352,000 km (90”) from the nucleus attributed by Stansberry et al. to nucleus rotation and instead propose that it is largely created by solar radiation pressure and gravity acting on micron-sized grains. We performed coma removal to the 16  $\mu\text{m}$  PU image in order to refine the nucleus’ emitted thermal flux. A new application of the Near Earth Asteroid Thermal Model at five wavelengths (5.730, 7.873, 15.80, 23.68, and 71.42  $\mu\text{m}$ ) was then used to refine SW1’s effective radius measurement to  $R = 32.3 \pm 3.1$  km and infrared beaming parameter to  $\eta = 1.1 \pm 0.2$ , respectively.

*Unified Astronomy Thesaurus concepts:* Comets (280); Short period comets (1452); Comae (271); Coma dust (2159); Infrared astronomy (786); Infrared telescopes (794); Dust continuum emission (412); Centaur group (215)

## 1. Introduction

29P/Schwassmann–Wachmann 1 (SW1) is a continuously active Centaur at the inner cusp of the Centaur-to-Jupiter-Family transition region and presents a rare opportunity to investigate activity drivers and ongoing material processing that occurs in a region too cold for vigorous water-ice sublimation. Recent dynamical simulations have shown that its current nearly circular trans-Jovian orbit (eccentricity, semimajor axis, and perihelion respectively:  $e = 0.04$ ,  $a = 6.03$  au, and  $q = 5.77$  au)<sup>8</sup> is typical for Centaurs in a short-lived transitional “gateway” from the outer solar system to the Jupiter-family comet (JFC) population (Sarid et al. 2019). Interestingly, despite SW1’s modest variation in energy input from the Sun, it frequently undergoes major outbursts superimposed on its normally present background, or “quiescent” coma (Larson 1980; Whipple 1980; Jewitt 1990; Trigo-Rodríguez et al. 2010; Kossacki & Szutowicz 2013; Hosek et al. 2013; Miles et al. 2016; Schambeau et al. 2017, 2019). Additionally, the CO production rate during periods of quiescent activity is more similar to long-period comets at similar heliocentric distances than to JFCs

(Bauer et al. 2015; Wierzechos et al. 2017; Womack et al. 2017; Bockelée-Morvan et al. 2021), and its dust outbursts may be uncorrelated with large fluctuations of its CO outgassing rate (Wierzechos & Womack 2020). Thus, questions naturally arise as to what activity drivers explain its enigmatic activity, and whether all JFCs experience a period of similar behaviors while they are in the gateway region. Are SW1’s activity behaviors reflective of outer solar system materials being thermally activated in the gateway, after a long period of cryogenic storage? Or are they an intrinsic property to it alone?

In 2015, we reported a new analysis of 2003 November Spitzer Infrared Array Camera 5.8 and 8.0  $\mu\text{m}$  and Multiband Imaging Photometer (MIPS) 24 and 70  $\mu\text{m}$  imaging, originally published by Stansberry et al. (2004). Using a new Spitzer data pipeline and intensive image processing techniques, the 2015 paper presented a new nucleus radius, beaming parameter, and infrared geometric albedo of SW1 (Schambeau et al. 2015). Subsequently, we determined that the Spitzer “blue” (i.e., at 16  $\mu\text{m}$ ) images obtained in the 2003 data set have sufficient coma detected for its analysis, modeling, and removal, and thus, they can provide new physical insights and constraints to SW1 models.

Here, for the first time, we present the Spitzer 16  $\mu\text{m}$  images and analyze them in the context of the 5.8, 8.0, 24, and 70  $\mu\text{m}$  data. We describe relevant observational details of the UT 2003 November epoch in Section 2. In Section 3.1, we present the characterization of thermal-infrared emission using the 16, 24,

<sup>8</sup> Minor Planet Circular (MPC) 111773.



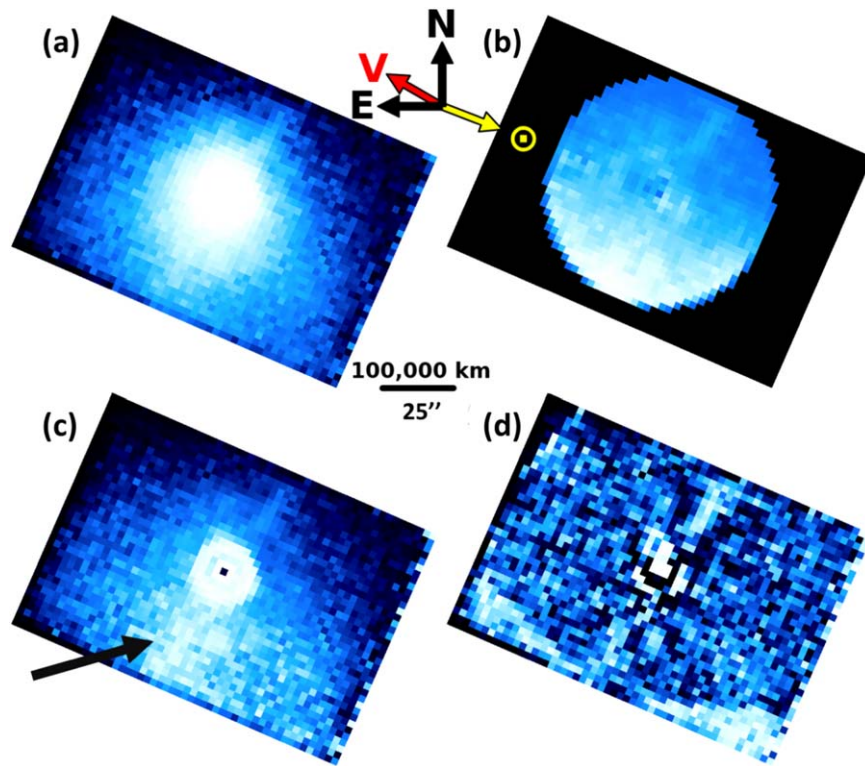


**Figure 1.** One of the Spitzer  $16\ \mu\text{m}$  blue PU images (with color scale black to blue to white indicating increasing surface brightness): (a) original image, (b) division by azimuthal average, (c)  $1/\rho$  profile removal, and (d) rotational shift differencing of  $18^\circ$  (Larson & Sekanina 1984; Samarasinha & Larson 2014). Equatorial north and east are indicated. The sky-plane-projected directions for the Sun and SW1’s heliocentric velocity vector are indicated by the yellow and red arrows, respectively. A black arrow on panel (c) indicates the slight coma enhancement in the south–southeast direction that is the south–southeast end of the 1–7 o’clock linear feature.

and  $70\ \mu\text{m}$  imaging data through coma morphology analysis, estimates of the  $\epsilon f\rho$  parameter, coma modeling of the dust grain size distribution and dust production rates for micron-sized and larger grains, and derivation of a coma color temperature map. In Section 3.2 we present an analysis of these images to provide a fifth nucleus photometry measurement at  $16\ \mu\text{m}$ . Using the five spectral flux density measurements of the nucleus, we implemented a Near Earth Asteroid Thermal Model (NEATM; Harris 1998) to derive a new measurement of the nucleus’ effective size and infrared beaming parameter ( $\eta$ ; a proxy for nucleus surface thermal inertia and/or surface roughness). In Section 4 we summarize our results and implications for SW1’s nucleus, quiescent large-grain coma, and activity state.

## 2. Observations

This work analyzes the Spitzer imaging data obtained with the  $16\ \mu\text{m}$  IRS blue peak-up (PU) and 24 and  $70\ \mu\text{m}$  MIPS instruments. Here we address the observational details of the  $16\ \mu\text{m}$  data and direct readers to our earlier work, Schambeau et al. (2015), for information on the 24 and  $70\ \mu\text{m}$  images.

During the Spitzer in-orbit checkout and science verification phase (Werner et al. 2004), SW1 was observed with the InfraRed Spectrograph (IRS; AORKEY: 6068992; Houck et al. 2004). Shortly before the IRS observations, blue-channel PU images were acquired in order to center SW1’s position on the detector’s “sweet spot” (the detector pixel location of the target’s centroid peak enabling optimal alignment and centering for the IRS slit). The blue PU channel of IRS’s Si:As array detector has dimensions of  $44 \times 31$  pixels, an effective monochromatic wavelength equivalent to  $15.8\ \mu\text{m}$ , and an effective pixel scale of

$1''.85/\text{pixel}$  in the detector’s  $X$  direction and  $1''.82/\text{pixel}$  in the detector’s  $Y$  direction. A total of six independent blue PU images were acquired: three images with SW1’s peak located on the center of the detector and three on the detector’s sweet spot, approximately 3 pixels away from the center of the array. Level 1 basic calibrated images were downloaded from the Spitzer Heritage Archive (SHA). An example image of SW1 located on the sweet spot is shown in Figure 1 along with enhanced images to highlight the coma’s morphology (Larson & Sekanina 1984; Samarasinha & Larson 2014). Table 1 provides a summary of the observational circumstances. The coma is slightly enhanced in the south–southeast direction and has a similar morphology to that seen in the MIPS  $24\ \mu\text{m}$  images, suggesting that the same particles are being measured in both bandpasses. Overall, aside from the slight increase in dust emission on the south–southeast side of the coma, as indicated by the division of an azimuthal average enhanced image (Figure 1(b)), the coma is lacking any defining coma morphology. A faint linear feature can be seen from approximately the 1 o’clock–7 o’clock positions.

For reference, the filter bandpasses of the  $16$ ,  $24$ , and  $70\ \mu\text{m}$  images are, respectively,  $13.3\text{--}18.7\ \mu\text{m}$ ,  $20.8\text{--}26.1\ \mu\text{m}$ , and  $60.9\text{--}80.6\ \mu\text{m}$ .

## 3. Image Analysis and Discussion

### 3.1. Thermal-infrared Coma Analysis

Thermal-infrared imaging of cometary dust comae allows for preferential probing of grain sizes on the order of microns and larger, such as those recorded with the IRS PU and MIPS, because smaller grains with  $2\pi a/\lambda < 1$ , where  $a$  is the grain radius, are inefficient emitters in the infrared (see Hanner et al. 1994;

**Table 1**  
Observations and Geometry Summary for UT 2003 November 23

Parameter	Value
Observations [Start:Stop]	[(07:15:32.960): (07:17:13.409)]
Exposure Time Per Image	9.44 s
Heliocentric Distance to SW1 ( $R_H$ )	5.73 au
Spitzer–SW1 Distance ( $\Delta$ )	5.54 au
Solar Phase Angle of SW1 ( $\alpha$ )	10°0
True Anomaly of SW1	342°8
Position Angle of the Sky-plane-projected Sun Direction <sup>a</sup>	248°2
Position Angle of the Sky-plane-projected Heliocentric Velocity Vector <sup>a</sup>	59°9

**Note.**

<sup>a</sup> The position angle is measured counterclockwise from north through east.

Lisse et al. 1998, 2004). Our Spitzer 16, 24, and 70  $\mu\text{m}$  images were analyzed to characterize the continuum emission created by micron-sized and larger grains in SW1’s quiescent dust coma. We note that micron- and submicron-sized grains also contain silicate emission bands between  $\sim 8$  and 13  $\mu\text{m}$  and at  $\sim 20$   $\mu\text{m}$ , which probably contribute a few percent to the flux in the 24  $\mu\text{m}$  images (see Schambeau et al. 2015, Figures 13 and 14). However, a detailed analysis of these emission features and their relatively minor impacts on the 24  $\mu\text{m}$  imaging is beyond the scope of our current work.

In this section we take advantage of these thermal-infrared images in combination with Spitzer’s stable and well-characterized point-spread function (PSF) in order to accurately isolate SW1’s dust coma flux contributions in each image. We assumed that the dominant grain sizes contributing to the detected flux in each band were approximately the size of their effective monochromatic bandpass wavelengths: 15.80, 23.68, and 71.42  $\mu\text{m}$  (as used by, e.g., Bauer et al. 2015, 2017).

To aid in the analysis of comae morphology, it is useful to reference an idealized “canonical” coma, containing an isotropic and steady-state emission of dust grains from the nucleus, with negligible dust grain fragmentation and solar radiation pressure. This canonical coma has a surface-brightness profile following a  $1/\rho$  behavior (where  $\rho$  is the sky-plane-projected cometocentric distance from the nucleus’s position) and is assumed in the derivation of the often-used  $Af\rho$  and  $\epsilon f\rho$  parameters (A’Hearn et al. 1984; Lisse et al. 2002; Kelley et al. 2013) that are described in more detail in Section 3.1.2. In practice the assumptions used to derive  $\epsilon f\rho$  break down for real comae, but its calculation provides a first-order estimate of comae dust production behaviors. SW1 experienced quiescent activity for at least two months surrounding the UT 2003 November epoch of Spitzer observations, based on Minor Planet Center (MPC) reported magnitude measurements,<sup>9</sup> so the canonical coma assumption is reasonable for these observations.

### 3.1.1. 16 and 24 $\mu\text{m}$ Coma Morphology

The 16  $\mu\text{m}$  blue PU images (Figure 1) were obtained 1.3 days before the 24  $\mu\text{m}$  MIPS images (Figure 2), which were obtained on UT 2003 November 24 15:05. The 16  $\mu\text{m}$  image’s coma did not display any clearly distinguishable large-scale radial or azimuthal features in either the unenhanced or

enhanced images. A slight enhancement on the south–southeast through southwest side of the coma is detected in the division by azimuthal average and the  $1/\rho$ -removed enhanced images (Figures 1(b) and (c)). This is further confirmed in Figure 3, which displays radial-surface-brightness profiles for position angles (PAs) at 45° spacings for the 16  $\mu\text{m}$  image. The radial profiles were generated by taking the median pixel value at a given radial position using 10° wide wedges center on the indicated PA. For comparison, each PA plot includes a radial profile for a scaled STINYTIM generated point-spread function (PSF; Krist 2006) representing how a detection of SW1’s bare nucleus would behave in the absence of a coma. A  $C/\rho^n$  functional form was fit to the profiles for  $\rho$  values between 14” and 30” for each PA (i.e., beyond any significant influence from the nucleus point source contribution), where  $C$  is a scaling constant representing the peak coma flux near the nucleus and  $n$  is the power index of the coma’s profile. The fitted profile power-law indices are listed in Table 2. Profiles for PAs spanning from the south-through-west directions, approximately centered on the projected sunward direction, have nearly canonical  $1/\rho$  coma profiles whereas profiles in the northeast have profile powers of approximately  $n=2$ . This asymmetric profile behavior is consistent with preferential emission of grains in the sunward direction (southwest).

The overall coma morphology as seen in the unenhanced 24  $\mu\text{m}$  (Figure 2(a)) image similarly shows an increased brightness in the southwest direction. This is further confirmed by the division by an azimuthal average and  $1/\rho$ -removed enhanced images. The rotational-shift-differenced enhanced image (Figure 2(d)) contains a curved wing feature that Stansberry et al. (2004) attribute to a rotating jet and from which they derived a  $\sim 60$  day rotation period for SW1’s nucleus. Taking into consideration the great similarity in the 16 and 24  $\mu\text{m}$  image morphology taken 1.3 days apart, and the relationship between the projected nucleus–Sun vector and the curved wing’s structure suggests that this feature is possibly not the result of nucleus rotation but is instead due to solar radiation pressure effects on micron-sized dust grains emitted in the sunward direction being turned back to form the dust tail in the northeast direction (Farnham & Schleicher 2005; Mueller et al. 2013; Li et al. 2014). While the  $\sim 60$  day rotation period derived by the earlier work may in fact coincidentally be reflective of SW1 potentially possessing a long rotation period (Miles et al. 2016; Schambeau et al. 2017, 2019), we propose that this curved wing feature is not the result of a slowly rotating nucleus. Interestingly, the wing would be symmetric around the sky-plane-projected nucleus–Sun axis for the case of isotropic emission from a localized nucleus surface area. Instead it is asymmetric, indicating a possible preferential direction for dust lofting from this source region.

Similar asymmetric curve-shaped features have long been seen in broadband visible imaging data of SW1 while undergoing major outbursts. Accounts of these coma morphologies have been reported in the early works of Jeffers (1956) and Roemer (1958). Whipple (1980) presents a detailed analysis of SW1’s outburst coma morphology as detected over a 50 yr baseline, resulting in the descriptive term of “ringtailed snorter” for this often seen curve-shaped feature. While it may at first seem appropriate to compare the outburst and quiescent coma morphologies, detailed analyses of SW1’s dust coma while in both phases of activity (Hosek et al. 2013; Miles et al. 2016; Schambeau et al. 2017, 2019) have provided descriptions of the underlying processes ongoing in both phases of activity and that

<sup>9</sup> Minor Planet Circulars: 49762, 49871, 49872, 49873, 50347, 50348.

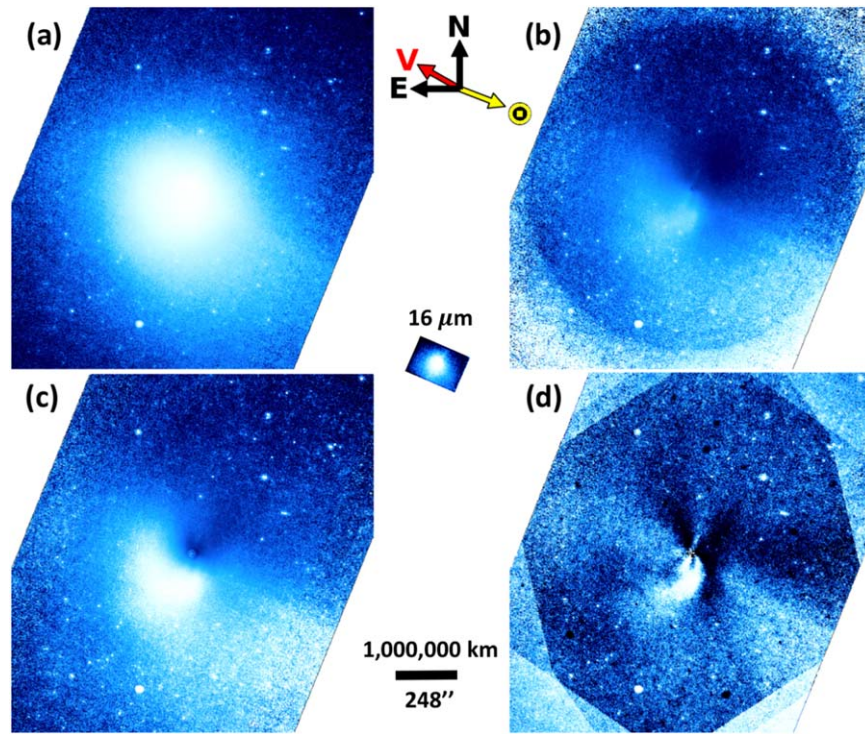


**Figure 2.** Shown is a cropped version of the  $24\ \mu\text{m}$  image (a), along with enhanced images: (b) division by an azimuthal average, (c)  $1/\rho$  profile removal, and (d) rotational shift differencing of  $18^\circ$ . Equatorial north and east are indicated. The sky-plane-projected directions for the Sun and SW1's heliocentric velocity vector are indicated by the yellow and red arrows. The  $16\ \mu\text{m}$  image (Figure 1(a)) is shown to highlight the differences in the field of views between the  $16$  and  $24\ \mu\text{m}$  images. The large-scale coma morphology shows an increased brightness in the southwest direction, possibly indicating preferential sunward emission. Also present are a more compact curved feature initially directed toward the south-southwest, curving toward the southeast, and a linear feature from the 1 o'clock to 7 o'clock position, similar to that in the  $16\ \mu\text{m}$  image.

the two are different. The morphology of the  $24\ \mu\text{m}$  quiescent coma's wing may resemble that of SW1's outburst coma; however, it was produced by different mechanisms (i.e., slow, sustained dust lofting with expansion velocities in the range of  $10\text{--}50\ \text{m s}^{-1}$ , while quiescent (Jewitt 1990) versus impulsive short-lived dust emission at high velocities in the  $100\text{--}300\ \text{m s}^{-1}$  range during major outbursts (Feldman et al. 1996; Trigo-Rodríguez et al. 2010; Schambeau et al. 2017, 2019)).

The outer edge of the wing feature seen in the  $24\ \mu\text{m}$  image in the southwest direction (Figure 2(d)) may indicate an approximate projected length for the turn-back distance of the grains from solar radiation pressure. Using a projected cometocentric distance of  $\sim 90''$  ( $352,000\ \text{km}$ ) for the turning point of the wing as the approximate turn-back distance and the Mueller et al. (2013) equation for turn-back distance due to solar radiation pressure, we estimate the dust coma's expansion velocity:

$$v = \left[ \frac{2\rho_g \beta g \sin \alpha}{(\cos \gamma)^2} \right]^{1/2}, \quad (1)$$

where  $\rho_g$  is the projected sky-plane turn-back distance of the dust grains,  $\gamma$  is the angle between the initial direction of the dust grains and the sky plane,  $\beta$  is the ratio of radiation pressure acceleration to acceleration due to solar gravity,  $\alpha$  is the solar phase angle of the observations, and  $g = GM_\odot/R_H^2$  is the solar gravitational acceleration on the dust grains ( $G$  is the gravitational constant,  $M_\odot$  is the Sun's mass, and  $R_H$  is the

heliocentric distance of the dust grains). We estimate a  $\beta$  value based on equations from Finson & Probst (1968) and Fulle (2004):

$$\beta = \frac{C_{\text{pr}} Q_{\text{pr}}}{\rho_d d}, \quad (2)$$

where  $C_{\text{pr}}$  is a collection of constants equal to  $3E_\odot/(8\pi cGM_\odot)$ , where  $E_\odot$  is the Sun's mean radiation. The parameter  $Q_{\text{pr}}$  is the scattering efficiency for radiation pressure for a dust grain of diameter  $d$ . Burns et al. (1979) provide a thorough description of  $Q_{\text{pr}}$  and explain that a value of  $Q_{\text{pr}} \approx 1$  is appropriate for the assumed  $d = 24\ \mu\text{m}$  grains here. We use a value for the dust grain bulk density based on recent spacecraft visited comae in situ measurements:  $\rho_d = 500\ \text{kg m}^{-3}$  (Fulle et al. 2016). With these assumptions we arrive at an estimated value of  $\beta = 0.096$ . The exact value for  $\gamma$  of the dust grains most dominantly contributing to the wing feature is unknown. Most probably it is the result of dust grains emitted over a continuum of angles. For this reason we calculate the outflow velocity for a range of sky-plane-projected dust grain angles:  $\gamma = 0^\circ$  ( $v = 50\ \text{m s}^{-1}$ ),  $\gamma = 45^\circ$  ( $v = 65\ \text{m s}^{-1}$ ), and  $\gamma = 80^\circ$  ( $v = 270\ \text{m s}^{-1}$ ).

A similar radial-surface-brightness profile analysis for the  $24\ \mu\text{m}$  image is shown in Figure 4. The overall appearance of the coma morphology is similar to that seen in the  $16\ \mu\text{m}$  image; however, the larger field of view (FOV) and higher S/N coma detection in the  $24\ \mu\text{m}$  image allow a more detailed investigation of the underlying processing ongoing within the

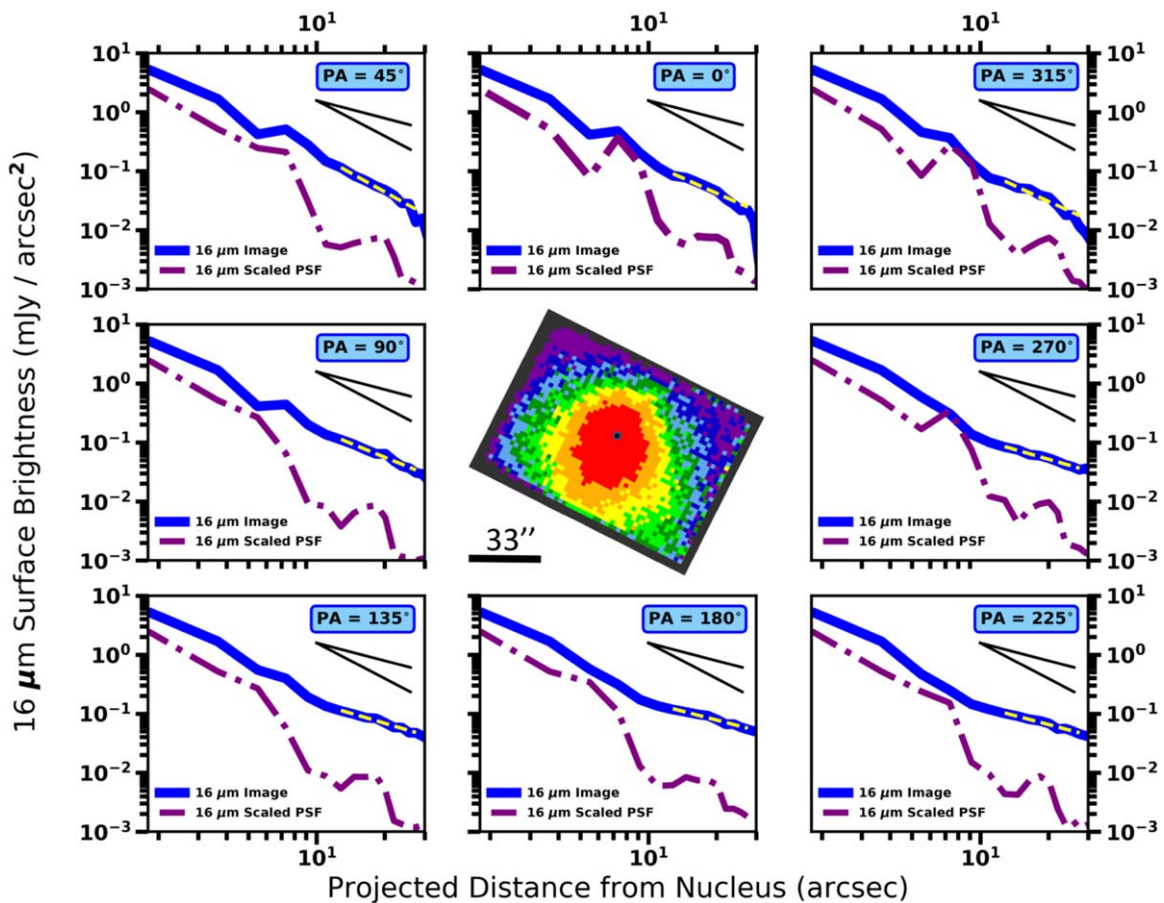


**Figure 3.** Radial profiles of the  $16\ \mu\text{m}$  image for different position angles in SW1. The  $16\ \mu\text{m}$  image is shown in the center of the plots for reference, with the location of the nucleus indicated by a black circle; the orientation of the image is equatorial north up and east to the left. Best-fit profiles are indicated by the yellow dashed lines for each PA and provided in Table 2. For reference, included in each plot are two black lines representing a  $1/\rho$  and  $1/\rho^2$  coma behavior. The “roller coaster” shaped profile for the PSF is the result of the Airy diffraction pattern of the space-based telescope.

**Table 2**  
16 and  $24\ \mu\text{m}$  Coma Profile Power-law Indices

Position Angle	$16\ \mu\text{m}$ ( $14''$ – $30''$ ) (56,000–120,000 km)	$24\ \mu\text{m}$ ( $14''$ – $30''$ ) (56,000–120,000 km)	$24\ \mu\text{m}$ ( $30''$ – $130''$ ) (120,000–520,000 km)	$24\ \mu\text{m}$ ( $200''$ – $470''$ ) (800,000–1,900,000 km)
$0^\circ$	–1.7	–1.1	–0.8	–1.4
$45^\circ$	–2.1	–0.9	–0.7	–1.5
$90^\circ$	–1.6	–0.7	–0.7	–1.5
$135^\circ$	–1.1	–0.6	–0.6	–1.7
$180^\circ$	–1.0	–0.7	–0.6	–1.1
$225^\circ$	–1.0	–0.6	–0.8	–0.8 <sup>a</sup>
$270^\circ$	–1.0	–0.9	–0.9	–0.9 <sup>a</sup>
$315^\circ$	–1.8	–0.9	–1.0	–1.0 <sup>a</sup>

**Note.**

<sup>a</sup> The coma surface-brightness profile power index between  $30''$  and  $470''$  was best fitted to a single value indicated in the column to the left.

dust coma. A change in slope of the profiles at a cometocentric distance of  $\sim 130''$  for PAs between  $0^\circ$  and  $180^\circ$  is suggestive of possible ongoing fragmentation for larger grains out to a projected cometocentric distance of 520,000 km (i.e.,  $\sim 130''$ ). This view is supported by the coma profile’s power-law index being shallower than  $-1$  interior to 520,000 km, suggesting an overabundance of dust grains interior to this projected distance when compared to a canonical steady-state dust emission. This behavior is possibly explained by a process of larger grains emitted from the nucleus and their subsequent fragmentation as they expand in the coma, or possibly from the decreasing size

via sublimation of larger icy grains losing their volatile content. In Section 3.1.4 we discuss the possibility of icy grains in more detail. These larger (0.1–1.0 mm) grain populations would not contribute significantly to the  $24\ \mu\text{m}$  coma cross section close to the nucleus because of its relative lack of surface area but could still easily support the observed number density of  $24\ \mu\text{m}$ -sized grains due to a fragmentation cascade (N.B.—as long as there are particles  $\gg 24\ \mu\text{m}$  in radius, they can always fragment/disrupt into many smaller particles and keep the observed particle size distribution (PSD) going) and thus maintain the coma’s enhanced  $24\ \mu\text{m}$  surface brightness.

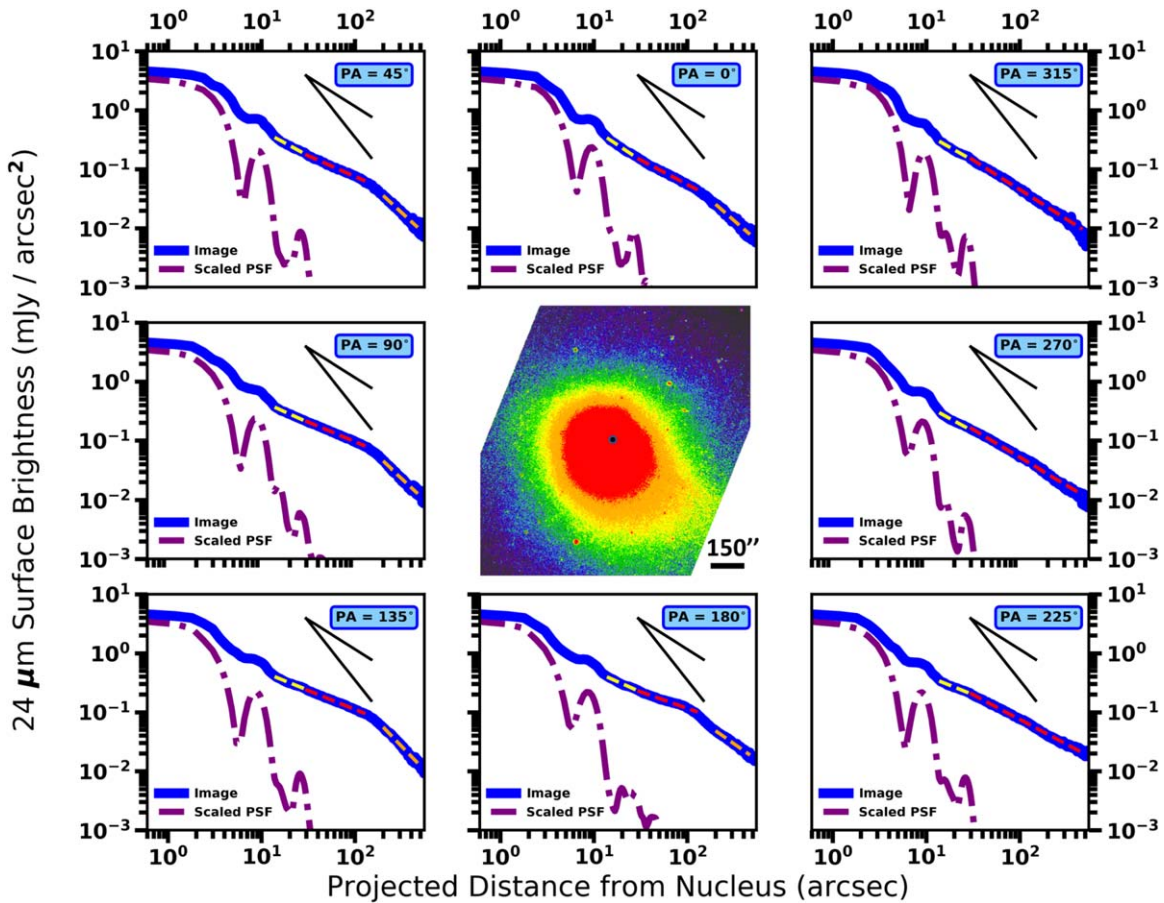


**Figure 4.** Radial profiles of the  $24\ \mu\text{m}$  image for different position angles. The coma morphology for radial profiles between  $0^\circ$  and  $180^\circ$  contains a knee-shaped feature at  $\rho \sim 130''$  (520,000 km) that is suggestive of a projected sky-plane length for ongoing coma grain fragmentation and/or the projected turn-back distance of dust grains from solar radiation pressure. Fitted power-law indices corresponding to the yellow, red, and orange curves are presented in Table 2. The location of the nucleus is indicated by the black circle in the center image. For reference, included in each plot are two black lines representing a  $1/\rho$  and  $1/\rho^2$  coma behavior. The roller-coaster-shaped profile for the PSF is the result of the Airy diffraction pattern of the space-based telescope.

Similar to the  $16\ \mu\text{m}$  image, the coma’s profiles in  $24\ \mu\text{m}$  close to the projected sunward direction (PAs:  $225^\circ$ ,  $270^\circ$ , and  $315^\circ$ ) all have a single profile index close to  $-1$ . A possible explanation for this constant surface brightness could be a preferential sunward emission of dust grains.

### 3.1.2. $\epsilon f\rho$ Measurements and Dust Production Estimates

For this analysis we calculated the  $\epsilon f\rho$  parameter (Lisse et al. 2002; Kelley et al. 2013), an often-used proxy for dust production rates using infrared emission that is analogous to the  $Af\rho$  parameter for reflected dust flux in the visible (A’Hearn et al. 1984). While the assumed canonical dust coma used to derive  $\epsilon f\rho$  is not valid for many comets, the utility of  $\epsilon f\rho$  comes from it establishing a standard procedure for estimating coma dust production rates and allowing a relative comparison between individual comets.

The expression for  $\epsilon f\rho$  used is

$$\epsilon f\rho(\lambda) = \frac{F_{\text{th}}(\lambda)}{\pi B(\lambda, T_c)} \times \frac{\Delta^2}{\rho}, \quad (3)$$

where  $\epsilon$  is the emissivity of the dust grains at wavelength  $\lambda$ ;  $f$  is a filling factor expressing the fraction of the photometry aperture containing dust grains;  $\rho$  is the linear aperture radius centered on the nucleus, which is being used to measure the

flux;  $F_{\text{th}}(\lambda)$  is the flux measured in the photometric aperture for wavelength  $\lambda$ ;  $B(\lambda, T_c)$  is the Planck function calculated at the color temperature  $T_c$  of the dust grains; and  $\Delta$  is the geocentric distance during the observation.

For the 2003 epoch of Spitzer SW1 imaging, we used properties for the dust coma derived from our earlier analysis of IRS observations of SW1. This analysis indicated the coma was dominated by submicron- to micron-sized amorphous silicate and amorphous carbon grains at a color temperature of  $\sim 140$  K (Schambeau et al. 2015). The color temperature map shown in Section 3.1.4 also indicates dust grains at similar color temperatures, but also that there is a color temperature structure present in the coma complicating the interpretation of a derived  $\epsilon f\rho$  based on an assumed dust coma with uniform temperature. With these understood limitations, we used Equation (3) to calculate  $\epsilon f\rho$  values for each of the three bands containing extracted coma flux measurements. Additionally, we calculated  $\epsilon f\rho$  values using an expression for dust coma color temperature ( $T_c = 300\ \text{K}/\sqrt{(R_H)} = 125\ \text{K}$ ) based on the results of the Survey of Ensemble Physical Properties of Cometary Nuclei (SEPPCoN) for JFC observations by Spitzer (Kelley et al. 2013) and for the case of grains at an ideal blackbody temperature ( $T_{\text{bb}} = 278\ \text{K}/\sqrt{(R_H)} = 117\ \text{K}$ ) for comparison. The IRS-derived and SEPPCoN-derived dust color temperatures are slightly hotter than an ideal blackbody at the same

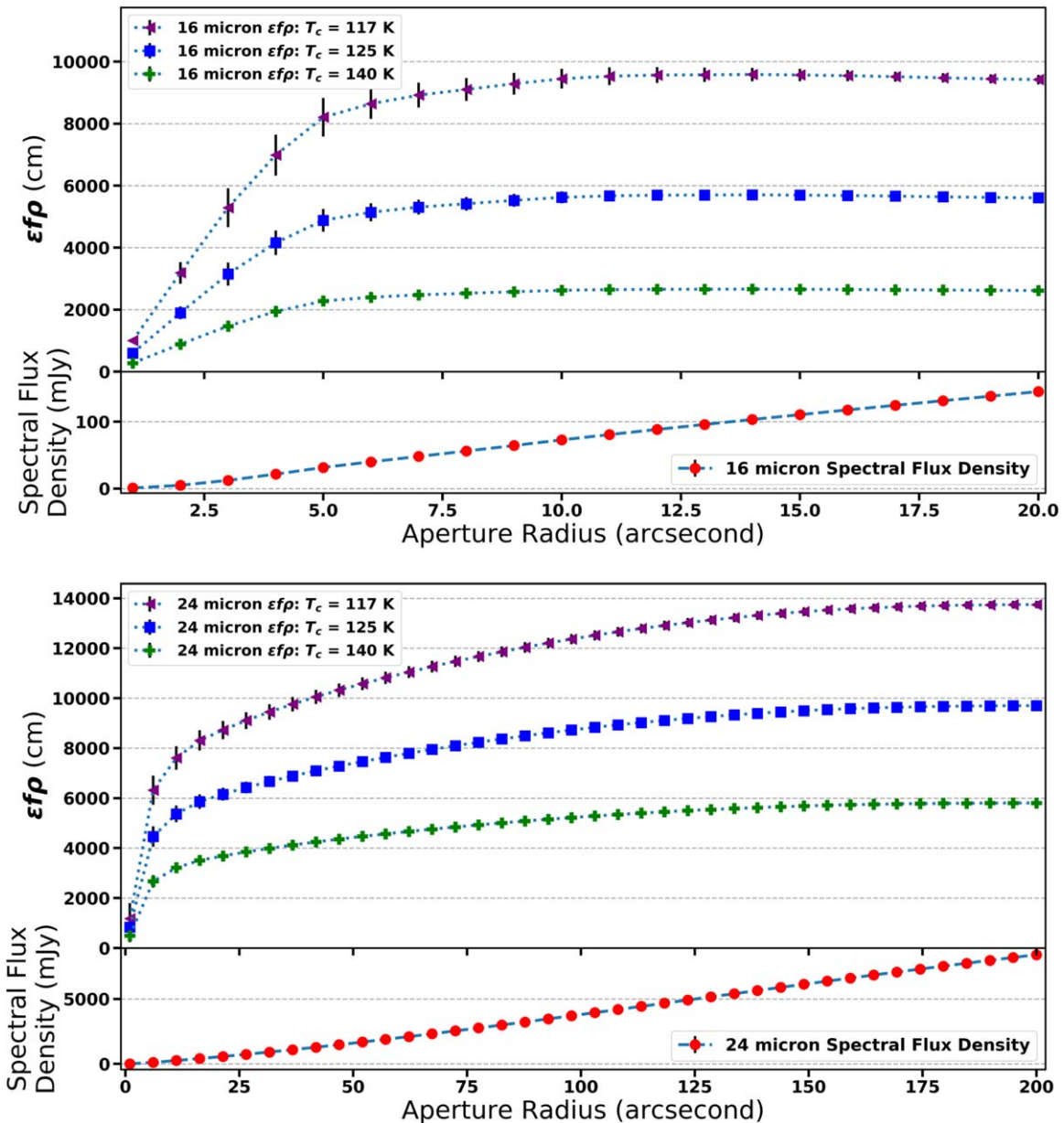


**Figure 5.** Top panel: SW1’s coma spectral flux density measurements and associated  $\epsilon f\rho$  measurements for the  $16\ \mu\text{m}$  image. Bottom panel: similar to the top, but for the  $24\ \mu\text{m}$  image. The  $16\ \mu\text{m}$  image appears to behave as a canonical dust coma with a semi-independent relationship between  $\epsilon f\rho$  and aperture size, while the  $24\ \mu\text{m}$  one has an increased value with increasing aperture size once past  $5''$ .

heliocentric distance. Most probably this is the result of superheated submicron-sized amorphous carbon grains present in the dust coma (Hanner et al. 1997) and/or potentially from the many emission features present in the thermal-infrared region (Wooden 2002; Markkanen & Agarwal 2019).

For  $F_{\text{th}}(\lambda)$  we subtracted the nucleus’s contribution to SW1’s overall flux in each aperture based on the scaled PSFs found during the coma removal process presented in Section 3.2. Additionally, flux from background sources (some of them serendipitously detected asteroids) was removed by interpolating the dust coma behavior for regions around each background source.

Figure 5 shows plots of the  $16$  and  $24\ \mu\text{m}$  measured spectral flux density values for an array of aperture radii along with their associated  $\epsilon f\rho$  measurements for the three color temperature

assumptions. Table 3 reports the measured flux and  $\epsilon f\rho$  values along with their associated uncertainties for the largest photometry apertures used for each image. The  $16\ \mu\text{m}$ ’s nearly constant  $\epsilon f\rho$  value for aperture radii larger than  $\sim 5''$  indicates that the 3D shape of the dust coma primarily contributing to this image maintains a nearly canonical spherical shape (Fink & Rubin 2012). On the other hand, the  $24\ \mu\text{m}$   $\epsilon f\rho$  profile has a slight positive slope indicating deviations from a canonical  $1/\rho$  coma’s expected aperture-independent constant value. The  $24\ \mu\text{m}$  slope behaviors support the possibility for an overabundance of  $24\ \mu\text{m}$ -sized dust grains for larger cometocentric distances. The steep decrease for  $\epsilon f\rho$  profiles for small apertures is an artifact of the coma’s image being the convolution of the coma’s intrinsic surface-brightness distribution with the telescope’s PSF (e.g., the intrinsic surface brightness is spread over a



**Table 3**  
SW1 Thermal-infrared Dust Coma Measurements

Band ( $\mu\text{m}$ )	$\rho^a$ ( $''$ )	Flux (mJy)	$\epsilon f\rho$ (cm)	$\dot{M}$ ( $\text{kg s}^{-1}$ )	$\epsilon f\rho$ (cm)	$\dot{M}$ ( $\text{kg s}^{-1}$ )	$\epsilon f\rho$ (cm)	$\dot{M}$ ( $\text{kg s}^{-1}$ )
$T_c = 117 \text{ K}$				$T_c = 125 \text{ K}$			$T_c = 140 \text{ K}$	
16	20	$145 \pm 2$	$9400 \pm 150$	$104 \pm 2$	$5600 \pm 90$	$124 \pm 2$	$2600 \pm 43$	$28.8 \pm 0.5$
24	20	$570 \pm 24$	$8700 \pm 360$	$144 \pm 6$	$6100 \pm 260$	$101 \pm 4$	$3700 \pm 150$	$61 \pm 3$
24	200	$8403 \pm 90$	$13700 \pm 150$	$227 \pm 3$	$9700 \pm 105$	$322 \pm 4$	$5800 \pm 63$	$96 \pm 1$
70	9	$102 \pm 50$	$2600 \pm 1300$	$130 \pm 65$	$2300 \pm 1100$	$113 \pm 55$	$1800 \pm 900$	$90 \pm 45$

**Note.**

<sup>a</sup> The radius of the sky-plane-projected photometry aperture.

larger projected surface area by the convolution process resulting in a decrease in integrated flux for apertures smaller than the PSF).

To verify that the difference in aperture photometry for the coma between the 16 and 24  $\mu\text{m}$  images is not the result of the local infrared background in each image, we compared coadded Wide-field Infrared Survey Explorer (WISE; Wright et al. 2010) backgrounds retrieved from the W3 (12  $\mu\text{m}$ ) and W4 (22  $\mu\text{m}$ ) intensity images downloaded from the NASA/IPAC Infrared Science Archive. W3 and W4 coadded images centered on the SW1's nucleus position during each epoch of imaging were compared, and we found no significant differences that could explain the different photometry behaviors.

The 70  $\mu\text{m}$  image's low-S/N surface-brightness coma detection did not allow a similar radial profile analysis. Instead, we report in Table 3 an updated 9'' radius aperture coma flux measurement. Our earlier reported 70  $\mu\text{m}$  flux density value (Schambeau et al. 2015) did not include an aperture correction for the measurement, so the earlier reported flux measurement is an underestimate. Based on a new reported measurement of  $103 \pm 50$  mJy, we calculated an  $\epsilon f\rho$  value. The large uncertainty in the derived 70  $\mu\text{m}$  coma flux measurement is due to the low S/N present in the mosaicked image and SW1's proximity to one of the jail-bar artifacts often present in MOPEX-generated mosaicked images (see Schambeau et al. 2015, Figure 2(b)).

We use the measured  $\epsilon f\rho$  values to estimate dust production rates during the Spitzer imaging according to

$$\dot{M} = (\epsilon f\rho) \times \frac{8a\rho_d v}{3\epsilon}, \quad (4)$$

where  $a$  is the radius of the grains,  $\rho_d$  is the density of the grains, and  $v$  is the radial velocity of the grains lofted from the nucleus's surface. For our calculations we assumed that the diameter of the grains dominating the emitted flux for each band is equal to the effective wavelength of each band: 15.8, 23.68, and 71.42  $\mu\text{m}$ . For the density of the grains we used the same value of  $\rho_d = 500 \text{ kg m}^{-3}$  (Fulle et al. 2016) that was used for the estimate of the dust expansion velocity. The velocity of the emitted dust grains was chosen to be  $50 \text{ m s}^{-1}$  based on the lower approximate values for dust expansion velocity from the 24  $\mu\text{m}$  coma morphology and turn-back distance from solar radiation pressure. While it is likely that larger grains will have slower radial velocities than smaller grains, we adopt the same value for each band, due to the observational uncertainties of the measurements. We use a

value for the dust emissivity of  $\epsilon = 0.95$ . Estimated dust production rates are presented in Table 3.

We have collected similar  $\epsilon f\rho$  measurements based on the SEPPCoN (Fernández et al. 2013; Kelley et al. 2013) and WISE/NEOWISE (Bauer et al. 2017) surveys for comets in order to compare SW1's measured values. Results from the WISE/NEOWISE survey (Bauer et al. 2017) enabled them to develop an empirical expression relating an expected thermal dust activity for an individual comet based on its nucleus size:

$$\log\left(\frac{\epsilon f\rho}{1 \text{ cm}}\right) = 3.5\left(1 - \exp\left(-\frac{D_N}{5.3 \text{ km}}\right)\right) + N(0, 0.25), \quad (5)$$

where  $D_N$  is the nucleus diameter in kilometers and  $N(0, 0.25)$  is a Gaussian distribution with a mean of 0 and variance of 0.25. In Figure 6, we plotted measurements from both infrared surveys, the empirical expression developed by Bauer et al. (2017), and SW1's measurements from this work.

As Figure 6 shows, Equation (5) fits the SEPPCoN  $\epsilon f\rho$  values and SW1 values presented in this work. Interestingly, the expression implies that comets with nuclei diameters larger than  $\sim 20$  km have a flattening of activity levels when compared to the steep increase of dust activity versus diameter for comets between 1 km to 10 km diameters. This may be partly due to an observational bias in favor of detecting larger nuclei at larger heliocentric distances in combination with the distant activity being driven by a process other than water ice sublimation. This comparison between SEPPCoN, NEOWISE, and SW1 values is new, and the good fit of Equation (5) to the observations indicates that the equation is a robust estimator of a comet's larger grain coma activity level.

Reports of SW1's dust production rate as derived from visible observations during periods of quiescent activity indicate a typical mass-loss rate for submicron-sized grains on the order of  $1\text{--}50 \text{ kg s}^{-1}$ . We arrived at these typical quiescent dust production rates using reported  $Af\rho$  measurements from Trigo-Rodríguez et al. (2010) and Hosek et al. (2013), but here we use a value of grain density  $\rho_d = 500 \text{ kg m}^{-3}$  in order to be consistent with our  $\epsilon f\rho$ -derived dust production rates. We note that these dust production rates are upper limits due to their calculated  $Af\rho$  values containing nucleus flux contributions. When compared to the estimated dust production rates as derived from the Spitzer data, which have nucleus flux contributions removed, the estimated dust production rates for grains in the range of 16–70  $\mu\text{m}$  have a higher mass-loss rate (Table 3) than the submicron-sized coma ( $< \mu\text{m}$  grains). It would be interesting to see if this trend of higher mass-loss rate for the tens of micron-sized grains is also

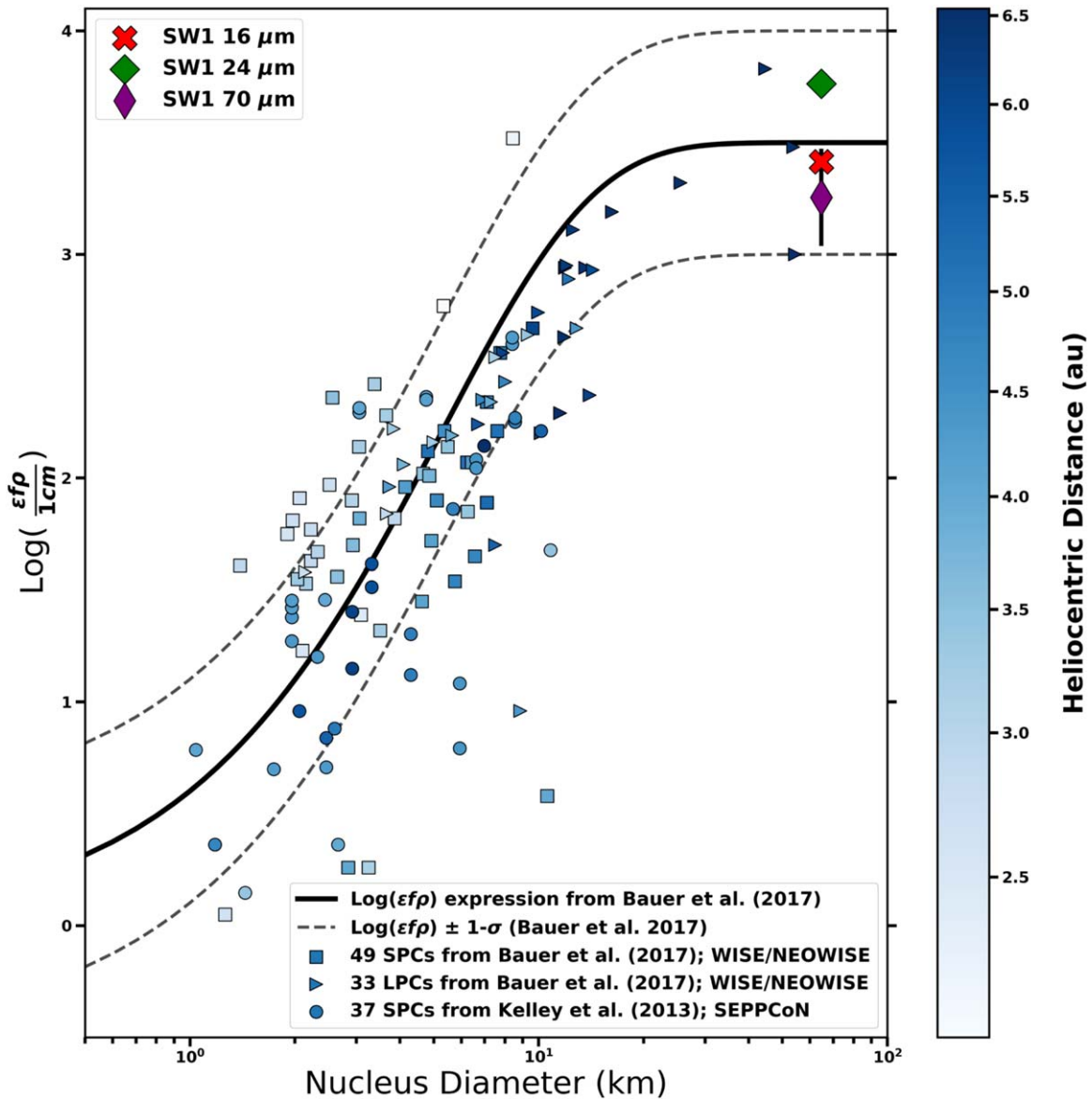


**Figure 6.** Comparison of measured  $\epsilon f \rho$  values versus nucleus diameter for comets and Centaurs from two infrared surveys and data presented here for SW1. The solid black curve indicates the empirically derived relation between  $\epsilon f \rho$  versus nucleus diameter presented in Bauer et al. (2017) using the WISE/NEOWISE-detected comets; see Equation (5) in this paper. Points for SW1 are based on the values from Table 3 for the dust temperature of  $T = 140$  K. Uncertainties for the  $16 \mu\text{m}$  and  $24 \mu\text{m}$  points are smaller than data markers. The colors of individual markers of the WISE/NEOWISE and SEPPCoN values indicate the comet’s heliocentric distance at the time of the  $\epsilon f \rho$  measurement. A color bar to the right of the figure indicates the heliocentric distance color scale.

seen during periods of major dust coma outburst (i.e., is the bulk of SW1’s outburst mass loss coming from grains that are on the order of 10s of microns to  $100 \mu\text{m}$  or from submicron-sized grains), enabling investigations of the quiescent versus outburst comae activity mechanisms.

### 3.1.3. Coma Modeling

Another approach to determine the dust production rate is to model the thermal emission of an ensemble of particles defined by its size distribution. We used the model described in Bockelée-Morvan et al. (2017), which computes the wavelength-dependent absorption coefficient and temperature of dust particles as a function of grain size using the Mie theory combined with an effective medium theory (EMT) in order to consider mixtures of different materials. EMTs allow us to calculate an effective refractive index for a medium made of a

matrix with inclusions of another material. The Maxwell–Garnett mixing rule is used in this model and is also applied to consider the porosity of the grains, set to be 50% at maximum (Bockelée-Morvan et al. 2017). The infrared thermal spectrum is computed by summing the contributions of the individual dust particles. The size distribution of the dust particles is described by a power-law  $n(a) \propto a^{-\beta}$ , where  $\beta$  is the size index, and the particle radius takes values from  $a_{\text{min}}$  to  $a_{\text{max}}$ . The dust density is taken equal to  $500 \text{ kg m}^{-3}$ . The effect of ice sublimation on the equilibrium grain temperature was not taken into account, as it has been shown that radiative cooling dominates overcooling by sublimation at far heliocentric distances (Beer et al. 2006).

We consider in this paper three different mixtures (see Bockelée-Morvan et al. 2017 for the references for optical constants): (1) a matrix of amorphous carbon with inclusions of amorphous olivine with an Fe:Mg composition of 50:50; (2) a

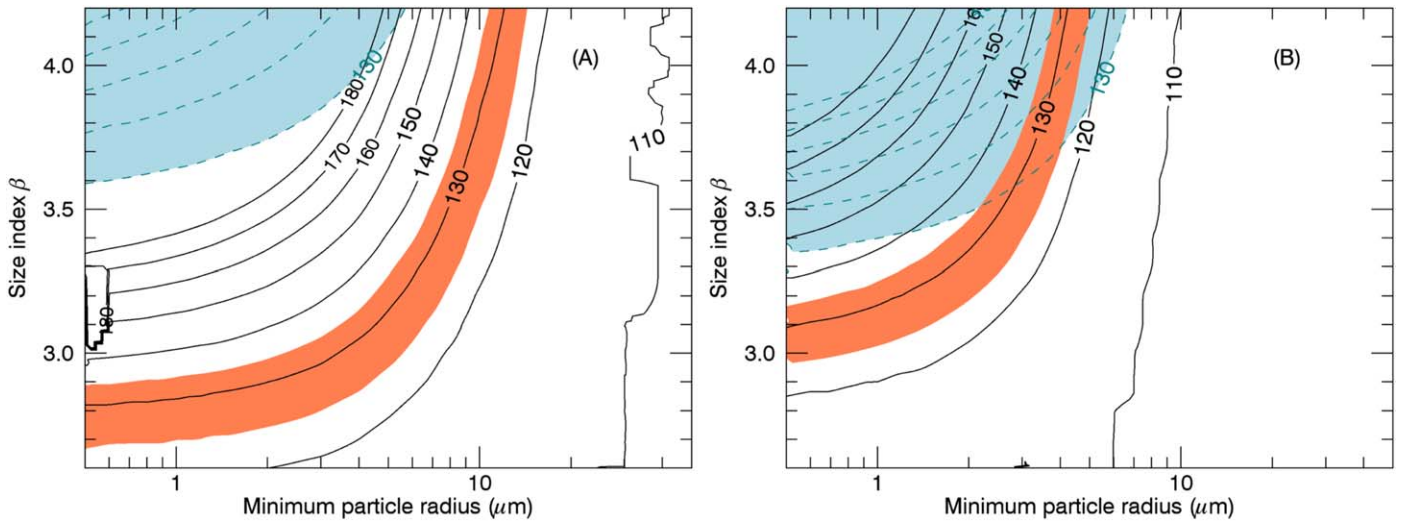


**Figure 7.** Modeled dust color temperatures  $T_{16/24}$ ,  $T_{24/70}$  as a function of minimum particle size and size index, for ice/carbon mixtures 2 (panel (A)) and 3 (panel (B)). Black solid lines show contours at constant  $T_{16/24}$ , in steps of 10 K. Blue dashed lines show contours at constant  $T_{24/70}$ , in steps of 10 K, for  $T_{24/70} \geq 130$  K. Color temperatures consistent with Spitzer-measured  $T_{16/24}$  and  $T_{24/70}$  values are colored in orange and blue, respectively. The assumed maximum particle size is  $a_{\text{max}} = 250 \mu\text{m}$ .

matrix of crystalline ice with inclusions of amorphous carbon; and (3) a matrix of amorphous carbon with inclusions of crystalline ice. For mixture (1) the carbon/olivine mass ratio is 1, a value consistent with the organic mass fraction measured in comet 67P dust particles (Bardyn et al. 2017). Mixtures (2) and (3) have the same ice fraction in a mass of  $\sim 45\%$  but have different optical properties.

Other parameters set in the model are the dust maximum size  $a_{\text{max}}$  and the dust velocity as a function of particle size, described as varying  $\propto a^{-0.5}$ , with a value of  $60 \text{ m s}^{-1}$  for  $10 \mu\text{m}$  particles. The maximum liftable size from the surface of SW1’s nucleus is estimated to be  $a_{\text{max}} = 250 \mu\text{m}$ , for a CO-driven activity restricted to a spherical segment with a half-angle of  $45^\circ$  and a total CO production rate of  $4 \times 10^{28} \text{ s}^{-1}$ , assuming our nucleus radius estimate of  $32.3 \text{ km}$  (Section 3.2) and a nucleus density of  $500 \text{ kg m}^{-3}$  (V. Zakharov 2021, personal communication; see Zakharov et al. 2018, 2021). This CO outgassing description is consistent with CO millimeter observations (Gunnarsson et al. 2008; Wierzbos & Womack 2020; Bockelée-Morvan et al. 2021).

The model was applied to simulate the flux density in a  $9''$  FOV radius at 16, 24, and  $70 \mu\text{m}$ , for comparison with Spitzer data. Simulations were made for a minimum dust particle size  $a_{\text{min}}$  in the range  $0.5\text{--}50 \mu\text{m}$  and size indices in the range  $2.5\text{--}4.6$ . These two parameters have indeed a strong influence on the dust thermal spectrum, with, e.g., a larger contribution from small particles for low  $a_{\text{min}}$  and high  $\beta$  values resulting in a higher dust color temperature. The Spitzer constraints are flux densities in a  $9''$  FOV radius of  $64 \pm 2 \text{ mJy}$ ,  $198 \pm 14 \text{ mJy}$ ,  $103 \pm 50 \text{ mJy}$  at 16, 24, and  $70 \mu\text{m}$ , respectively. This corresponds to the color temperatures of  $T_{16/24} = 129 \pm 5 \text{ K}$ , based on the 16 and  $24 \mu\text{m}$  fluxes, and  $T_{24/70} = 177^{+52}_{-47} \text{ K}$  based on the 24 and  $70 \mu\text{m}$  fluxes.  $T_{16/24}$  and  $T_{24/70}$  are consistent within  $1\sigma$  with a value of  $\sim 130 \text{ K}$ , but the high central value of  $T_{24/70}$  resulting from the relatively faint  $70 \mu\text{m}$  flux might suggest an excess of small particles poorly radiating at long wavelengths.

Figure 7 shows isocontours of  $T_{16/24}$  (black plain lines) and  $T_{24/70}$  (dashed blue lines) as a function of  $a_{\text{min}}$  and  $\beta$ . Domains consistent with measured  $T_{16/24}$  and  $T_{24/70}$  values are filled in orange and blue colors, respectively. We only show results for

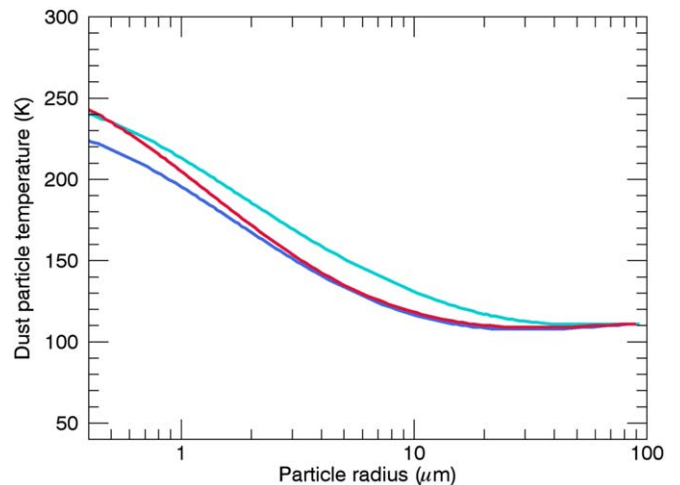


**Figure 8.** Temperature of the dust particles as a function of particle radius. Results for mixtures 1 (matrix of carbon with ice inclusions), 2 (matrix of ice with carbon inclusions), and 3 (matrix of carbon with olivine inclusions) are shown in blue, turquoise, and red, respectively.

ice-carbon mixtures (2) and (3), because results for the carbon-silicate mixture (1) are similar to those obtained for mixture (3). For mixtures (1) (not shown) and (3), the orange and blue domains overlap for  $a_{\text{min}} = 2\text{--}5 \mu\text{m}$ , whereas no overlapping is observed for mixture (2) for any set of  $(a_{\text{min}}, \beta)$ . Grains made of mixture (2) are hotter than other mixtures for sizes below  $30 \mu\text{m}$  (Figure 8), and this explains the different infrared spectra.

In Figure 9, we show dust production rates derived from the  $24 \mu\text{m}$  flux density using the  $(a_{\text{min}}, \beta)$  parameters that provide  $T_{16/24}$  values consistent with the measured value, i.e., those defining the orange region in Figure 7. For mixtures (1) and (3) with matrices of amorphous carbon, the range is  $50\text{--}200 \text{ kg s}^{-1}$ . The low end is obtained for the highest  $(a_{\text{min}}, \beta)$  values ( $= (5 \mu\text{m}, 4.1\text{--}4.4)$ ), which is a steep size distribution where  $5\text{--}10 \mu\text{m}$  grains dominate the infrared emission. For size distributions with

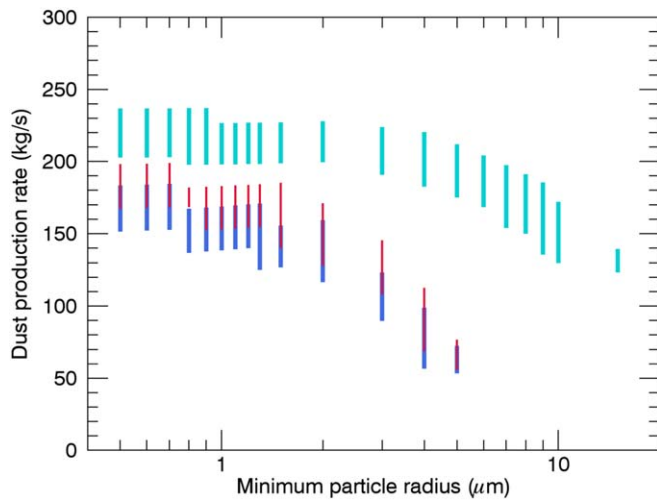


**Figure 9.** Dust production rates derived from the  $24\ \mu\text{m}$  flux density measured in a  $9''$  FOV radius, using  $(a_{\min}, \beta)$  parameters providing color temperature  $T_{16/24}$  values consistent with the measured value of  $129 \pm 5\ \text{K}$ . The range of production rate values for a given minimum size reflects the range of  $\beta$  values fulfilling the requirement and the uncertainty in the  $24\ \mu\text{m}$  flux. Results for mixtures 1, 2, and 3 are shown in blue, turquoise, and red, respectively.

$a_{\min} = 4\text{--}5\ \mu\text{m}$ , the dust production rates deduced from the  $24$  and  $70\ \mu\text{m}$  fluxes are consistent, and in the range  $50\text{--}100\ \text{kg s}^{-1}$ . However, this is not the case for size distributions with small  $a_{\min}$  values (and consequently low  $\beta$  values; Figure 7), for which  $70\ \mu\text{m}$  derived dust production rates are by a factor of 2–3 lower than those deduced from the  $24\ \mu\text{m}$  flux. For the ice/carbon mixture 2 (matrix of crystalline ice), the dust production rate inferred from the  $24\ \mu\text{m}$  flux is between  $130$  and  $240\ \text{kg s}^{-1}$  (Figure 9). The values derived from the  $70\ \mu\text{m}$  flux are more than two times lower for all sets of  $(a_{\min}, \beta)$  parameters. This is an expected result because for this composition, the model fails in reproducing both the  $T_{16/24}$  and  $T_{24/70}$  values.

The dust production rates derived with model parameters leading to a satisfactory fit to data ( $50\text{--}100\ \text{kg s}^{-1}$ ) are in overall agreement with those estimated in Section 3.1.2 using a simple approach. The Mie scattering model shows that measuring dust fluxes at several wavelengths in the thermal IR can provide constraints on the PSD and thermal properties. The obtained results are here limited due to the low-S/N of the  $70\ \mu\text{m}$  dust coma flux. A flaw in the present analysis is also the known limitations of the Mie scattering theory and of the Maxwell–Garnett mixing rule for modeling dust spectra (Lien 1990; Mishchenko & Travis 2008).

### 3.1.4. Coma Color Temperature Map

In Figure 10, a color temperature map of the coma based on the  $16$  and  $24\ \mu\text{m}$  images is shown. This was generated by using the spectral flux density values of the coma after removal of flux contributions from the nucleus; the procedure of nucleus versus coma flux contributions is described in Section 3.2 for the  $16\ \mu\text{m}$  image and in our earlier work (Schambeau et al. 2015) for the  $24\ \mu\text{m}$  data. Masked pixels identified by the teal square near the center represent regions where the PSF’s subtraction may have resulted in a significant over- or undersubtraction for individual pixels. The white pixels on the top-left and top-right of the color map are not “hot” but instead are masked as white due to the low-S/N  $16\ \mu\text{m}$  detections resulting in negative spectral flux density pixel

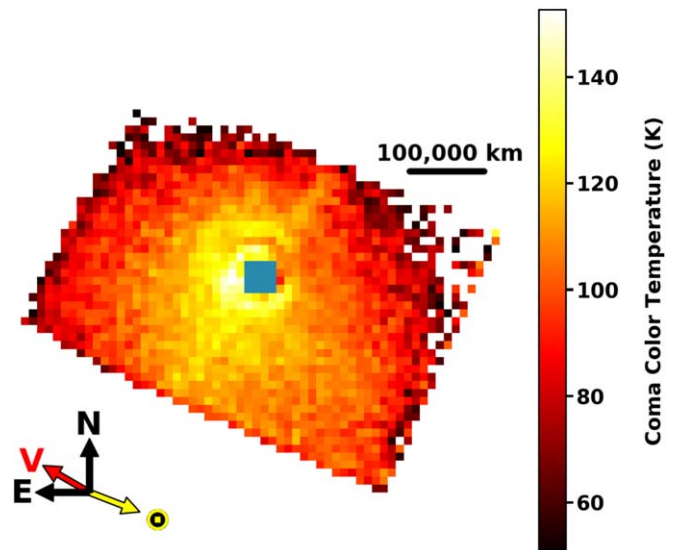


**Figure 10.** Coma color temperature map based on the  $16$  and  $24\ \mu\text{m}$  images.

values after background subtraction. These pixels have been excluded from the color temperature fitting procedure. We note that the actual temperatures of the grains most probably are different from the values derived from fitting a Planck blackbody profile to the individual pixel values from the  $16$  and  $24\ \mu\text{m}$  images due to the silicate emission features present in the  $24\ \mu\text{m}$  bandpass and the dust coma PSD (Wooden 2002; Markkanen & Agarwal 2019). The peak temperature of the grains of  $\sim 140\ \text{K}$  close to the nucleus is in agreement with a color temperature derived from the IRS spectrum as analyzed in Schambeau et al. 2015.

Overall, the general trend is a decreasing color temperature with increasing projected distance away from the nucleus. The eastern half of the coma has a higher temperature than the western side by  $\sim 20^\circ$ . The interpretation of this behavior is uncertain based on the current Spitzer imaging data. We mention here plausible explanations for these color temperature behaviors based on the properties of the dust coma. One possible explanation can be a population of relatively smaller grains on the eastern side of the coma composing the tail that are less efficient at radiating their stored thermal energy. Another possibility is that the western side of the coma has a higher abundance of submicron-sized grains, resulting in an enhanced  $24\ \mu\text{m}$  emission above that of an ideal blackbody due to the silicate emission bands around  $20\ \mu\text{m}$ . The overall impact of this behavior would be a slightly lower color temperature for the western side of the coma. Future modeling efforts may be able to select between the combination of processes driving the observed color temperature but are beyond the scope of this current work.

Using the color temperature as a proxy for the approximate dust grain temperatures and the results of Beer et al. (2006) indicates that for grain sizes on the order of tens of microns, as we have here for the  $16$  and  $24\ \mu\text{m}$  images, the grains have a dust mass fraction for water ice ( $X$ , where  $X = 1$  for pure water ice) in the range of 25%–50%, with smaller grains having a higher ice content. We calculated the expected lifetimes for the water-ice content of assumed spherical icy grains with diameters equal to  $16$ ,  $24$ , and  $70\ \mu\text{m}$  and dust mass fractions  $X_{16} = 0.5$ ,  $X_{24} = 0.40$ , and  $X_{70} = 0.25$  (Mukai 1986; Lien 1990; Beer et al. 2006). The lifetimes of the water-ice content of the

grains are, respectively, 112, 154, and 373 days. For these estimated lifetimes we have ignored the increased temperatures of grains as their sizes decrease due to the ongoing water-ice sublimation, so our derived lifetimes are estimated upper limits.

The presence of grains containing water ice has been inferred by the increased emissivity at longer wavelengths as derived from the modeling of SW1's Spitzer IRS spectrum (Schambeau et al. 2015). Additionally, SW1's H<sub>2</sub>O production rates as derived from Herschel/HIFI observations indicate a nonnuclear extended source that is explained by the sublimation of an icy grain coma (Bockelée-Morvan et al. 2021). The H<sub>2</sub>O measured production rates based on AKARI and Herschel observations are in the range of  $Q_{\text{H}_2\text{O}} \sim 3\text{--}7 \times 10^{27}$  molecules s<sup>-1</sup> (Ootsubo et al. 2012; Bockelée-Morvan et al. 2021). These measured production rates are the same order of magnitude as what would be produced by the sublimation of icy grains if we use the dust-to-ice mass fractions as constrained from their color temperature and the dust production rates derived from  $\epsilon f \rho$ . As a first-order estimate of the coma's  $Q_{\text{H}_2\text{O}}$  due to the sublimation of icy grains, we calculated the production rate that would be produced from the sublimation of the water ice content of icy grains following the dust production rates presented in Table 3. Assuming that all of the water-ice content for individual grains is fully sublimated, we arrive at an estimated range of  $Q_{\text{H}_2\text{O}} \sim (1\text{--}3) \times 10^{27}$  molecules s<sup>-1</sup>, supporting the argument that the measured water production rates may be explained by a nonnuclear source of icy grains in the coma.

### 3.2. Nucleus Spectral Flux Density Measurements and a New NEATM

To obtain nucleus photometry measurements from the blue PU images, the flux from SW1's coma was modeled and removed. We used a well-established coma modeling technique (Lamy & Toth 1995; Fernandez 1999; Lisse et al. 1999) for this procedure, where the azimuthal coma behavior is measured in regions outside of significant contribution from the nucleus' PSF in order to generate a synthetic coma model. The model coma's flux contribution is then subtracted from the observations resulting in an approximately bare-nucleus residual image. The residual image is then used to scale an STINYTIM generated PSF (Krist 2006) to represent the nucleus's total flux. The reader is referred to our previous work (Schambeau et al. 2015) for a detailed description of this procedure.

The coma modeling and removal procedure was applied to each of the PU images resulting in six independent nucleus photometry measurements from six images at an effective 15.8  $\mu\text{m}$  wavelength. The individual color corrected measurements are: 84.1, 85.0, 85.0, 87.5, 89.6, and 88.4 mJy, with a typical uncertainty of  $\pm 7$  mJy. The final measurement used for thermal modeling analysis was taken as the average of the individual measurements:  $86 \pm 2$  mJy, with the stated  $1\sigma$  uncertainty being the standard deviation of the six measurements.

Figure 11 shows the new 15.8  $\mu\text{m}$  measurement plotted along with the other four Spitzer nucleus photometry values that we reported earlier (Schambeau et al. 2015). We also plot the best-fitting four-band thermal model (NEATM; Harris 1998) that we used in the earlier work to extract the nucleus's effective radius  $R = 30.2^{+3.7}_{-2.9}$  km and beaming parameter  $\eta = 0.99^{0.26}_{-0.19}$ . A refit using the now five spectral flux density measurements produces a nucleus size estimate and infrared beaming parameter that are slightly larger, but within the  $1\sigma$  uncertainties of the earlier results:  $R = 32.3 \pm 3.1$  km and

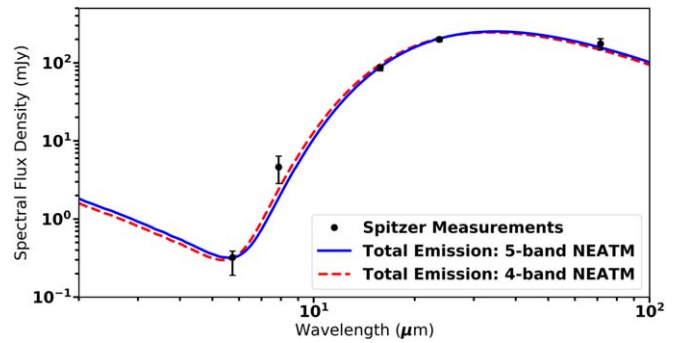


**Figure 11.** Five spectral flux density measurements of SW1, incorporating the new blue PU data at 16  $\mu\text{m}$ , all acquired during 2003 November with Spitzer. Also shown is a new five-band NEATM, which produces a nucleus radius estimate and infrared beaming parameter of  $R = 32.3 \pm 3.1$  km and  $\eta = 1.1 \pm 0.2$ , along with the previous four-band NEATM from Schambeau et al. (2015). Uncertainties are  $1\sigma$ . The consistently higher than fit value for the 8  $\mu\text{m}$  measurement may be the result of enhanced emission due to silicate emission bands in this region.

$\eta = 1.1 \pm 0.2$ . We propose these new values be used in future investigation of SW1 in lieu of our earlier analysis (Schambeau et al. 2015), because of the reduced uncertainty due to modeling with five, rather than four, points. For our new NEATM analysis similar assumptions to those used for our previous work and for (e.g.,) SEPPCoN (Fernández et al. 2013) were used: bolometric bond albedo  $A = 0.012$  (assuming a visible-wavelength geometrical albedo  $p = 0.04$  and phase integral relation  $q = 0.290 + 0.684G$ , (Harris & Lagerros 2002), emissivity  $\epsilon = 0.95$ , and slope parameter  $G = 0.05$ .

## 4. Summary and Conclusions

A more detailed analysis of the 2003 November Spitzer observations of SW1 (Schambeau et al. 2015) is presented, which incorporates 16  $\mu\text{m}$  data for the first time and significantly improves characterization of the Centaur's tens of microns dust coma during a period of quiescent activity.

The 16  $\mu\text{m}$  blue PU images were remarkably symmetric, with evidence for a  $\sim 70\%$  coma enhancement in the south-southeast direction, which may be reflective of tail formation. The 16  $\mu\text{m}$  coma's morphology indicated preferential sunward emission of dust grains. No signs of grain fragmentation were indicated by the data within the image FOV ( $273,000 \times 386,000$  km).

Reanalysis of the 24  $\mu\text{m}$  images reveals a large-scale coma morphology of increased brightness in the southwest direction, consistent with preferential sunward emission. These data also show a more compact wing feature initially directed toward the south-southwest to a projected cometocentric distance of 352,000 km ( $90''$ ) and curving toward the southeast. This feature has previously been interpreted to be due to the nucleus's rotation, but we propose instead that this is the result of solar radiation pressure effects and gravity on micron-sized dust grains that were emitted in the sunward direction and were turned back to form a dust tail. Further analysis of this feature is encouraged. Interestingly, analysis of the 24  $\mu\text{m}$  surface-brightness radial profiles shows a noticeable change of slope at  $\sim 520,000$  km cometocentric distance at positions angles of  $\sim 0^\circ$  through  $180^\circ$ . This change in slope is consistent with the projected distance to the outer edge of the curved feature. We used measurements of this turning-back point of the curved feature to estimate a dust grain outflow velocity in the range of  $50\text{--}270$  m s<sup>-1</sup> depending on the ejection direction of grains.

Using the improved 140 K color temperature measured from the IRS spectrum (Schambeau et al. 2015) and in this work (Section 3.1.4), we calculated the  $\epsilon\rho$  parameters:  $16\ \mu\text{m}$  ( $2600 \pm 43\ \text{cm}$ ),  $24\ \mu\text{m}$  ( $5800 \pm 63\ \text{cm}$ ), and  $70\ \mu\text{m}$  ( $1800 \pm 900\ \text{cm}$ ). SW1's values were found to follow the  $\epsilon\rho$  versus nucleus size relation observed from the WISE/NEOWISE-observed comets (Bauer et al. 2017). Additionally, for the first time, we compare the WISE/NEOWISE- and SEPPCoN- derived (Kelley et al. 2013)  $\epsilon\rho$  measurements and see agreement between the two surveys, strengthening the argument for the empirically derived relationship's application as a predictor of cometary comae.

A coma model (Bockelée-Morvan et al. 2017) was used to constrain the coma's dust grain size distribution and mass-loss rate. The model was constrained by  $9''$  radius aperture photometry measurements of the  $16$ ,  $24$ , and  $70\ \mu\text{m}$  coma flux density. Models with a dust grain composition of a matrix of amorphous carbon with inclusions of (1) amorphous olivine or (2) crystalline water ice were in agreement with the Spitzer data. The two models had similar ranges for the best-fit grain size distributions: power-law index  $\beta$  ranging from 4.1 to 4.4, minimum grain size  $a_{\text{min}}$  ranging from 4 to  $5\ \mu\text{m}$ , and maximum grain radius  $a_{\text{max}} = 250\ \mu\text{m}$ . The dust production rates derived with model parameters leading to a satisfactory fit to data ( $50\text{--}100\ \text{kg s}^{-1}$ ) are in overall agreement with those estimated using the measured  $\epsilon\rho$  values.

Using the  $16$  and  $24\ \mu\text{m}$  images we constructed a coma color temperature map, which also peaks at  $\sim 140\ \text{K}$ , decreasing with increasing cometocentric distance, and an east-to-west asymmetry with the eastern coma being  $\sim 20^\circ$  higher. This behavior is the result of a PSD of grains of varying compositions. Future analyses of these data are encouraged to better constrain SW1's large-grain coma environment.

We used the  $140\ \text{K}$  color temperature as a plausible physical temperature for individual grains. This assumption is supported by our earlier analysis of the IRS spectrum (Schambeau et al. 2015). Using the dust production rates measured here we estimated a  $\text{H}_2\text{O}$  production rate from the sublimation of icy coma grains:  $Q_{\text{H}_2\text{O}} \sim (1\text{--}3) \times 10^{27}\ \text{molecules s}^{-1}$ . This range agrees with other measurements of SW1's water production rate (Ootsubo et al. 2012; Bockelée-Morvan et al. 2021).

Coma modeling and its removal from the IRS blue PU imaging data at  $16\ \mu\text{m}$  were used, along with measurements at other infrared wavelengths, to produce a nucleus radius of  $R = 32.3 \pm 3.1\ \text{km}$  for SW1, which is within  $1\sigma$  of and has smaller uncertainties than prior measurements using Spitzer data (Stansberry et al. 2004, 2008; Schambeau et al. 2015). This analysis also yields a slightly higher NEATM derived beaming parameter ( $\eta = 1.1 \pm 0.2$ ). The size of SW1 places it on the smaller end of the currently known Centaur size distribution (Bauer et al. 2013; Lellouch et al. 2013; Duffard et al. 2014), but on the larger end for small bodies with known cometary activity (Stansberry et al. 2008; Fernández et al. 2013). With the refined nucleus size estimate presented here, we encourage future modeling efforts to better understand the bound inner coma environment of SW1.

The Centaur SW1's large size among active objects, in combination with its orbital history that indicates it has not spent a significant amount of time interior to Jupiter (Sarid et al. 2019), positions it as a high-priority target for future observational and in situ investigations to better understand moderately sized and relatively pristine planetesimals to better

understand the period of thermal evolution experienced while in the gateway transition from Centaur to JFC. We encourage the community to undertake new observations of SW1 and also for any currently existing and planned new observations to be listed on the SW1 observing campaign website: [wirtanen.astro.umd.edu/29P/29P\\_obs.shtml](http://wirtanen.astro.umd.edu/29P/29P_obs.shtml). Additionally, we provide here links to the following resources emphasizing the importance of continued observations of SW1 and best practices for new observations: (1) the call for observations from Womack et al. (2020) and (2) a guide for new observations provided by the British Astronomical Association (Miles 2019).

We would like to thank Dr. Richard Miles for his helpful discussions during the preparation of this manuscript. Additionally, we would like to thank our two anonymous reviewers, whose thorough review of the manuscript provided improvements to the presentation of the analyses.

We also thank the NASA Earth and Space Science Fellowship (NNX16AP41H) and the Center for Lunar and Asteroid Surface Science (CLASS, NNA14AB05A) for support of this work.

This work is based on observations made with the Spitzer Space Telescope, which is operated by the Jet Propulsion Laboratory, California Institute of Technology under a contract with NASA. This research made use of Tiny Tim/Spitzer, developed by John Krist for the Spitzer Science Center. The Center is managed by the California Institute of Technology under a contract with NASA. This publication makes use of data products from the Wide-field Infrared Survey Explorer, which is a joint project of the University of California, Los Angeles, and the Jet Propulsion Laboratory/California Institute of Technology, funded by the National Aeronautics and Space Administration.


## ORCID iDs

Charles A. Schambeau  <https://orcid.org/0000-0003-1800-8521>

Yanga R. Fernández  <https://orcid.org/0000-0003-1156-9721>

Nalin H. Samarasinha  <https://orcid.org/0000-0001-8925-7010>

Maria Womack  <https://orcid.org/0000-0003-4659-8653>

Dominique Bockelée-Morvan  <https://orcid.org/0000-0002-8130-0974>

Carey M. Lisse  <https://orcid.org/0000-0002-9548-1526>

Laura M. Woodney  <https://orcid.org/0000-0002-0004-7381>

## References

- A'Hearn, M. F., Schleicher, D. G., Millis, R. L., Feldman, P. D., & Thompson, D. T. 1984, *AJ*, 89, 579
- Bardyn, A., Baklouti, D., Cottin, H., et al. 2017, *MNRAS*, 469, S712
- Bauer, J. M., Grav, T., Blauvelt, E., et al. 2013, *ApJ*, 773, 22
- Bauer, J. M., Grav, T., Fernández, Y. R., et al. 2017, *AJ*, 154, 53
- Bauer, J. M., Stevenson, R., Kramer, E., et al. 2015, *ApJ*, 814, 85
- Beer, E. H., Podolak, M., & Prrialnik, D. 2006, *Icar*, 180, 473
- Bockelée-Morvan, D., Biver, N., Zakharov, V., et al. 2021, *A&A*, in preparation
- Bockelée-Morvan, D., Rinaldi, G., Erard, S., et al. 2017, *MNRAS*, 469, S842
- Burns, J. A., Lamy, P. L., & Soter, S. 1979, *Icar*, 40, 1
- Duffard, R., Pinilla-Alonso, N., Santos-Sanz, P., et al. 2014, *A&A*, 564, A92
- Farnham, T. L., & Schleicher, D. G. 2005, *Icar*, 173, 533
- Feldman, P., McPhate, J. B., Weaver, H. A., Tozzi, G.-P., & A'Hearn, M. F. 1996, *BAAS*, 28, 1084
- Fernandez, Y. R. 1999, PhD thesis, Univ. Maryland College Park

- Fernández, Y. R., Kelley, M. S., Lamy, P. L., et al. 2013, *Icar*, **226**, 1138
- Fink, U., & Rubin, M. 2012, *Icar*, **221**, 721
- Finson, M. J., & Probstein, R. F. 1968, *ApJ*, **154**, 327
- Fulle, M., Marzari, F., Della Corte, V., et al. 2016, *ApJ*, **821**, 19
- Fulle, M. 2004, in *Motion of Cometary Dust*, ed. M. C. Festou, H. U. Keller, & H. A. Weaver (Tucson, AZ: Univ. Arizona Press), 565
- Gunnarsson, M., Bockelée-Morvan, D., Biver, N., Crovisier, J., & Rickman, H. 2008, *A&A*, **484**, 537
- Hanner, M. S., Gehrz, R. D., Harker, D. E., et al. 1997, *EM&P*, **79**, 247
- Hanner, M. S., Lynch, D. K., & Russell, R. W. 1994, *ApJ*, **425**, 274
- Harris, A. W. 1998, *Icar*, **131**, 291
- Harris, A. W., & Lagerros, J. S. V. 2002, *Asteroids in the Thermal Infrared* (Tucson, AZ: Univ. Arizona Press), 205
- Hosek, M. W. J., Blaauw, R. C., Cooke, W. J., & Suggs, R. M. 2013, *AJ*, **145**, 122
- Houck, J. R., Roellig, T. L., van Cleve, J., et al. 2004, *ApJS*, **154**, 18
- Jeffers, H. M. 1956, *AJ*, **61**, 380
- Jewitt, D. 1990, *ApJ*, **351**, 277
- Kelley, M. S., Fernández, Y. R., Licandro, J., et al. 2013, *Icar*, **225**, 475
- Kossacki, K. J., & Szutowicz, S. 2013, *Icar*, **225**, 111
- Krist, J. 2006, *Tiny Tim/Spitzer User's Guide* (2nd ed.; Pasadena, CA: Spitzer Science Center)
- Lamy, P. L., & Toth, I. 1995, *A&A*, **293**, L43
- Larson, S. M. 1980, *ApJL*, **238**, L47
- Larson, S. M., & Sekanina, Z. 1984, *AJ*, **89**, 571
- Lellouch, E., Santos-Sanz, P., Lacerda, P., et al. 2013, *A&A*, **557**, A60
- Li, J.-Y., Samarasinha, N. H., Kelley, M. S. P., et al. 2014, *ApJL*, **797**, L8
- Lien, D. J. 1990, *ApJ*, **355**, 680
- Lisse, C. M., A'Hearn, M. F., Fernández, Y. R., & Peschke, S. B. 2002, in *IAU Coll. 181, Dust in the Solar System and Other Planetary Systems Vol. 15*, ed. S. F. Green et al. (Oxford: Pergamon Press), 259
- Lisse, C. M., A'Hearn, M. F., Hauser, M. G., et al. 1998, *ApJ*, **496**, 971
- Lisse, C. M., Fernández, Y. R., A'Hearn, M. F., et al. 2004, *Icar*, **171**, 444
- Lisse, C. M., Fernández, Y. R., Kundu, A., et al. 1999, *Icar*, **140**, 189
- Markkanen, J., & Agarwal, J. 2019, *A&A*, **631**, A164
- Miles, R. 2019, *Observing the Outbursting Comet 29P/Schwassmann-Wachmann*, <https://britastro.org/node/18562>
- Miles, R., Faillace, G. A., Mottola, S., et al. 2016, *Icar*, **272**, 327
- Mishchenko, M. I., & Travis, L. D. 2008, *BAMS*, **89**, 1853
- Mueller, B. E. A., Samarasinha, N. H., Farnham, T. L., & A'Hearn, M. F. 2013, *Icar*, **222**, 799
- Mukai, T. 1986, *A&A*, **164**, 397
- Ootsubo, T., Kawakita, H., Hamada, S., et al. 2012, *ApJ*, **752**, 15
- Roemer, E. 1958, *PASP*, **70**, 272
- Samarasinha, N. H., & Larson, S. M. 2014, *Icar*, **239**, 168
- Sarid, G., Volk, K., Steckloff, J. K., et al. 2019, *ApJL*, **883**, L25
- Schambeau, C. A., Fernández, Y. R., Lisse, C. M., Samarasinha, N., & Woodney, L. M. 2015, *Icar*, **260**, 60
- Schambeau, C. A., Fernández, Y. R., Samarasinha, N. H., Mueller, B. E. A., & Woodney, L. M. 2017, *Icar*, **284**, 359
- Schambeau, C. A., Fernández, Y. R., Samarasinha, N. H., Woodney, L. M., & Kundu, A. 2019, *AJ*, **158**, 259
- Stansberry, J., Grundy, W., Brown, M., et al. 2008, in *Physical Properties of Kuiper Belt and Centaur Objects: Constraints from the Spitzer Space Telescope*, ed. M. A. Telescopio et al. (Tucson, AZ: Univ. Arizona Press), 161
- Stansberry, J. A., Van Cleve, J., Reach, W. T., et al. 2004, *ApJS*, **154**, 463
- Trigo-Rodríguez, J. M., García-Hernández, D. A., Sánchez, A., et al. 2010, *MNRAS*, **409**, 1682
- Werner, M. W., Roellig, T. L., Low, F. J., et al. 2004, *ApJS*, **154**, 1
- Whipple, F. L. 1980, *AJ*, **85**, 305
- Wierzchos, K., & Womack, M. 2020, *AJ*, **159**, 136
- Wierzchos, K., Womack, M., & Sarid, G. 2017, *AJ*, **153**, 230
- Womack, M., Sarid, G., Harris, W., Wierzchos, K., & Woodney, L. 2020, *MPBu*, **47**, 350
- Womack, M., Sarid, G., & Wierzchos, K. 2017, *PASP*, **129**, 031001
- Wooden, D. H. 2002, *EM&P*, **89**, 247
- Wright, E. L., Eisenhardt, P. R. M., Mainzer, A. K., et al. 2010, *AJ*, **140**, 1868
- Zakharov, V. V., Ivanovski, S. L., Crifo, J. F., et al. 2018, *Icar*, **312**, 121
- Zakharov, V. V., Rodionov, A. V., Fulle, M., et al. 2021, *Icar*, **354**, 114091